



# Modification of aluminum current collectors with laser-scribed graphene for enhancing the performance of lithium ion batteries

Er-Chieh Cho<sup>a</sup>, Cai-Wan Chang-Jian<sup>b,\*\*\*</sup>, Yen-Ju Wu<sup>c</sup>, Szu-Han Chao<sup>d</sup>, Jen-Hsien Huang<sup>e</sup>, Kuen-Chan Lee<sup>f,\*\*\*\*</sup>, Huei Chu Weng<sup>g,\*\*</sup>, Shih-Chieh Hsu<sup>d,h,\*</sup>

<sup>a</sup> Department of Clinical Pharmacy, School of Pharmacy, College of Pharmacy, Taipei Medical University, 250 Wuxing Street, Taipei City, 110, Taiwan

<sup>b</sup> Department of Mechanical and Automation Engineering, I-Shou University, No.1, Sec. 1, Syuecheng Rd., Dashu District, Kaohsiung City, 84001, Taiwan

<sup>c</sup> International Center for Young Scientists (ICYS), National Institute for Materials Science (NIMS), 1-2-1 Sengen, Tsukuba, Ibaraki, 305-0047, Japan

<sup>d</sup> Department of Chemical and Materials Engineering, Tamkang University, No. 151, Yingzhuan Road, Tamsui District, New Taipei City, 25137, Taiwan

<sup>e</sup> Department of Green Material Technology, Green Technology Research Institute, CPC Corporation, No.2, Zuonan Rd., Nanzi District, Kaohsiung City, 81126, Taiwan

<sup>f</sup> Department of Science Education, National Taipei University of Education, No.134, Sec. 2, Heping E. Rd., Da-an District, Taipei City, 106, Taiwan

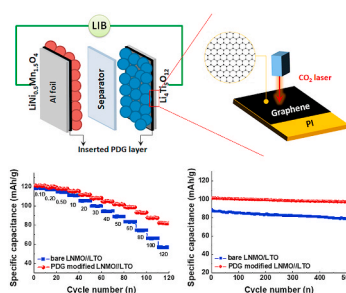
<sup>g</sup> Department of Mechanical Engineering, Chung Yuan Christian University, No. 200, Chungpei Road, Chungli District, Taoyuan City, 32023, Taiwan

<sup>h</sup> Water Treatment Science and Technology Research Center, Tamkang University, No. 151, Yingzhuan Road, Tamsui District, New Taipei City, 25137, Taiwan

## HIGHLIGHTS

- Graphene-modified Al foils are prepared using laser writing technique.
- Graphene-coated Al foils are used as a current collector in lithium ion battery.
- Graphene layer can enhance the adhesion and conductivity.
- The inserted graphene layer can enhance the rate and cycling performance.

## GRAPHICAL ABSTRACT



## ARTICLE INFO

### Keywords:

Graphene  
Laser irradiation  
Current collector  
Lithium ion battery

## ABSTRACT

In this study, the graphene-modified Al foils are prepared to assemble lithium ion batteries (LIBs) through a three-step approach comprising: (1) deposition of the polyamic acid (PAA) on the Al substrate; (2) curing the PAA to form the polyimide (PI)-coated Al foils; (3) converting the PI into porous graphene by  $\text{CO}_2$  laser irradiation. With integration of the PI derived graphene (PDG) in the LIBs, the inserted PDG layer can enhance the adhesion and interface resistance between the active layer and Al electrode. The  $\text{LiNi}_{0.5}\text{Mn}_{1.5}\text{O}_4$  (LNMO)// $\text{Li}_4\text{Ti}_5\text{O}_{12}$  (LTO) full cells with PDG layer are also fabricated to evaluate the effect of the modified layer on the cell performance. Compared to the pristine Al electrode, the modified current collector can improve the rate

\* Corresponding author. Department of Chemical and Materials Engineering, Tamkang University, No. 151, Yingzhuan Road, Tamsui District, New Taipei City, 25137, Taiwan.

\*\* Corresponding author.

\*\*\* Corresponding author.

\*\*\*\* Corresponding author.

E-mail addresses: [cwchangjian@isu.edu.tw](mailto:cwchangjian@isu.edu.tw) (C.-W. Chang-Jian), [klee@tea.ntue.edu.tw](mailto:klee@tea.ntue.edu.tw) (K.-C. Lee), [hcweng@cycu.edu.tw](mailto:hcweng@cycu.edu.tw) (H.C. Weng), [roysos@mail.tku.edu.tw](mailto:roysos@mail.tku.edu.tw) (S.-C. Hsu).

<https://doi.org/10.1016/j.jpowsour.2021.230060>

Received 8 March 2021; Received in revised form 15 May 2021; Accepted 18 May 2021

Available online 26 June 2021

0378-7753/© 2021 Elsevier B.V. All rights reserved.

performance and reduce the temperature rise during the charge/discharge process leading to better cycling stability.

## 1. Introduction

With the recent development of environmental awareness, renewable energy sources have been viewed as a potential means of alleviating the risks associated with high consumption of fossil fuel. Clean and renewable energy sources can help to reduce the greenhouse gas emissions and create a sustainable society. However, the power output of renewable energy sources is unstable and depend on weather conditions. Therefore, reliable energy storage systems (ESS) have become a key partner of renewable energy sources such as photovoltaic solar, wind, and hybrid power plants, especially in areas that are not connected to a strong grid [1]. Among the various energy storage technologies, LIBs hold great promise due to their high energy density, remarkable rate performance and prolonged cycling life [2–4]. These features make LIBs suitable for the ESS to address the intermittency of solar and wind power.

A typical LIB has a two-electrode configuration, which is composed of cathode materials and anode materials deposited on a metal current collector separated by an electrolyte and a separator. In general, the commercial Al foils with smooth surface has limited contact area and poor adhesion between active material and Al electrode leading to high contact resistance and poor rate performance. During the charging/discharging process, the commercial Al foil can be corroded by the organic electrolytes [5,6]. Moreover, the addition of organic acids during the electrode processing to enhance the dispersion of active materials is also possible to form a passivation layer ( $\text{Al}_2\text{O}_3$ ) on the Al electrode [7]. These issues usually produce additional impedance between active material and metallic current collector leading to the poor electrochemical performance. Furthermore, the corrosions of Al foil occurred during long-term cycling are also considered to be bottleneck for next-generation high voltage LIBs. Recently, some efforts have been made to resolve the above-mentioned problems, including construction of nanostructured Al foil [8], formation of the crosslinking between active layer and Al electrode [9], deposition of conducting polymer on the Al electrode [10] and surface modified Al foil with a carbon-based coating, including conductive carbon [11–13], carbon nanotube [14] and graphene [15–18]. Among these approaches, the modification of Al foils with a carbon layer is the most competitive strategy to enhance the LIB performance due to its simple process, chemical stability and superior conductivity.

Recently, the PI derived graphene (PDG) with high conductivity has been prepared via the laser scribing [19–22]. During the laser irradiation, the rapid local heating can transform the PI into graphene accompanied by gas emissions such as  $\text{CO}_2$ ,  $\text{NO}_2$  and  $\text{H}_2\text{O}$ . This process would dramatically rise the internal pressure which results in the three-dimensional (3D) porous graphene structure. These gases generated during the process can produce high internal pressure leading to a 3D porous graphene structure. The unique structure of the PDG make it a promising candidate for the development of 3D graphene coated Al foil in the application of LIBs. The porous hierarchical structure can increase the interfacial area between active material and electrode leading to better adhesion and lower resistance. The inserted PDG layer also can prevent the Al corrosion caused by organic electrolyte during the long-term cycling. In this article, we have demonstrated stable, high rate LNMO//LTO full cells assembled using the PDG modified Al electrodes as the current collector. Compared with the bare Al current collector, the LIB fabricated with PDG modified Al electrodes displays remarkable

performance with a better rate capability, lower temperature rises and enhanced cycling life.

## 2. Experimental section

### 2.1. Preparation of PDG modified Al foils

The copolycondensation-type PAA was synthesized using pyromellitic dianhydride and oxydianiline as monomers by the known method described in the previous work [23]. The PAA solution in NMP was deposited on the Al foils by the doctor-blade coating. The PAA/Al substrates were heated at  $100\text{ }^\circ\text{C}$  under vacuum for 1 h to remove the solvent. The films were thermally cured by heating at  $350\text{ }^\circ\text{C}$  for 1 h in  $\text{N}_2$  atmosphere to complete the imidization reaction and form the PI/Al substrates. PDG films were prepared with a laser platform (Universal Laser Systems, VLS2.3), equipped with a  $10.6\text{ }\mu\text{m}$   $\text{CO}_2$  laser (30 W). All the samples were prepared under ambient conditions using 15 W of laser power with a scan rate of  $40\text{ mm/s}$  and beam size of  $\sim 250\text{ }\mu\text{m}$ . The working distance was controlled at  $0.5\text{ mm}$ .

### 2.2. Preparation of LTO and LNMO materials

The microspherical LTO powders were prepared by spray-dried approach synthesized according to the procedure reported previously [24]. Typically,  $\text{TiO}_2$  and  $\text{Li}_2\text{CO}_3$  were mixed in de-ionized water with a circulation-type wet grinder (JUSTNANO JBM-C020) for 8 h. Then, the mixture was slowly pumped into pilot spray dryer (OHKAWARA KAKOHKI Co., LTD, model L-8i, No. 145874) and the outlet temperature was maintained at  $120\text{ }^\circ\text{C}$ . The as-prepared precursor was further calcined at  $800\text{ }^\circ\text{C}$  for 2 h to obtain the microspherical LTO powders. The  $\text{Ni}_{0.25}\text{Mn}_{0.75}(\text{OH})_2$  powders were prepared through co-precipitation method which used as precursor to synthesize the LNMO synthesized according to the procedure reported previously [25]. In brief,  $\text{NiSO}_4 \cdot 6\text{H}_2\text{O}$  and  $\text{MnSO}_4 \cdot \text{H}_2\text{O}$  were dissolved in de-ionized water and the resultant solution was transferred to a reactor at  $50\text{ }^\circ\text{C}$ . At the same time, a chelating agent consisted of  $\text{NH}_4\text{OH}$  and  $\text{NaOH}$  aqueous solution was fed into the reactor drop by drop to maintain pH at 10.5. The obtained  $\text{Ni}_{0.25}\text{Mn}_{0.75}(\text{OH})_2$  precursor was washed and dried and finally mixed with  $\text{Li}_2\text{CO}_3$  before thermally annealing in air at  $750\text{ }^\circ\text{C}$  for 12 h to obtain LNMO.

### 2.3. Characterization

The crystalline structure was characterized by X-ray powder diffraction (XRD) using a Bruker D2 PHASER. The functional groups of the PAA and PI were determined using Fourier transform infrared (FTIR) spectroscopy (Thermo Nicolet iS5) in the  $4000\text{--}600\text{ cm}^{-1}$  range. The morphology of the PDG are investigated by scanning electron microscope (SEM, JEOLJSM 6701F) and transmission electron microscope (TEM, JEOL 2010). Raman spectrum of the PDG was measured with a Raman spectrometer (HR800, HORIBA). The molecular weight of PAA was determined by gel permeation chromatography (GPC) analysis (Viscotek GPC system, TDA 302) two columns (KF806) using  $670\text{ nm}$  laser as the incident light source. The GPC measurement was performed using NMP as eluent at a flow rate of  $0.8\text{ mL/min}$ . During the GPC measurement, the whole system was maintained at  $60\text{ }^\circ\text{C}$ . Thermogravimetric analyses (TGA) were carried out by a Q50, TA instrument, using

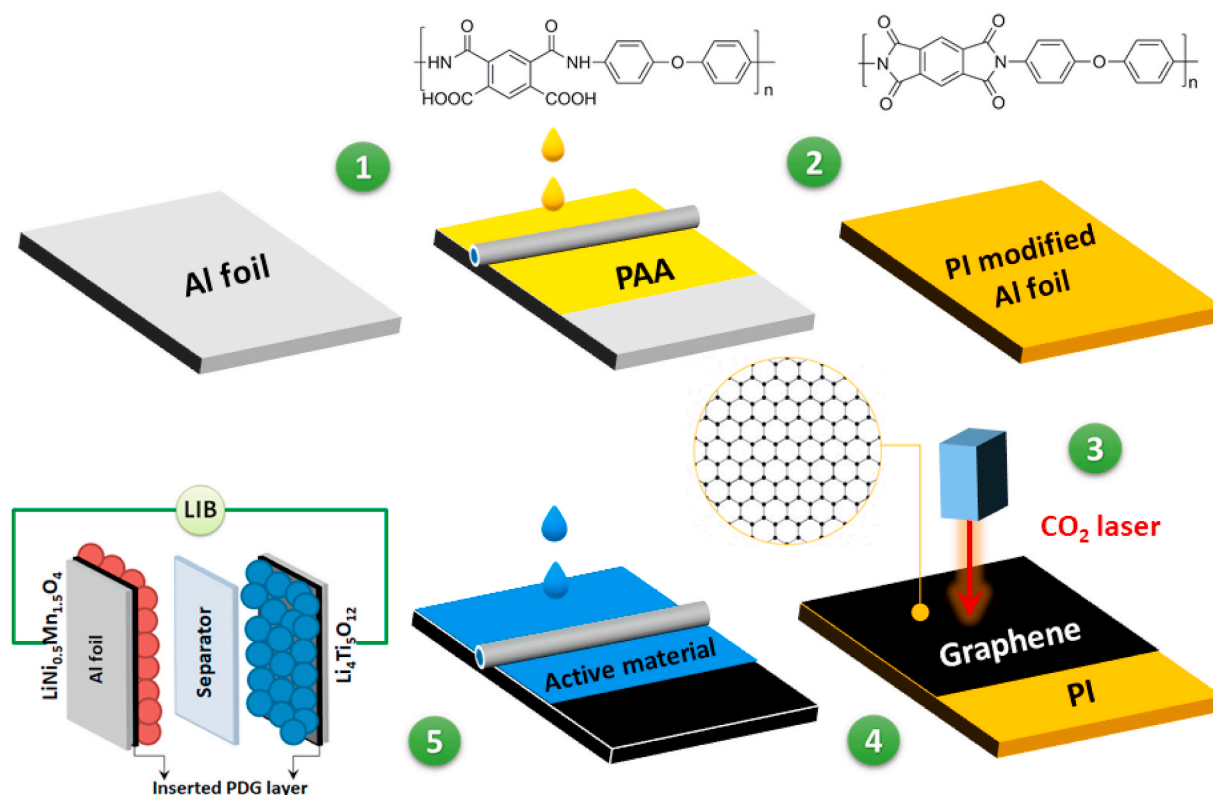


**Fig. 1.** Schematic illustration of the preparation of PDG-incorporated LIBs. (1) The PAA was first cast onto the Al foil via doctor-blade coating method; (2) the PAA/Al substrates were thermally treated at 350 °C under a N<sub>2</sub> atmosphere to convert the PAA into PI structure. (3) with the CO<sub>2</sub> laser irradiation, the PI can be converted into PDG; (4) deposition of active layer on the PDG/Al electrode; (5) LIB assembling process.

a heating rate of 10 °C min<sup>-1</sup> in N<sub>2</sub> atmosphere. The adhesion strength for the LTO electrodes with a size of 2 × 2 cm<sup>2</sup> was measured with a force gauge (DS2-1000 N Model, IMADA). The material and interface resistances of the electrode were obtained using a multipoint probe system (RM2610, HIOKI Corp., Japan) at room temperature. The temperature and IR-image of the LNMO//LTO full cells were recorded by an infra-red thermograph (TiX 1000).

#### 2.4. Electrochemical characterization

The chemical composition of cathode and anode slurries includes 85 wt% active material, 10 wt% conductive carbon and 5 wt% binder. All the materials are well-mixed in NMP via a 3D mixer (BiO-COMPO-NENTS™ Inversina 2L) to obtain the slurry. The slurries were then cast on bare and PDG modified Al foils, dried at 100 °C under vacuum and roll pressed. Before the cell assembling, the pressed electrode was punched into disks (1.13 cm<sup>2</sup>) further dried under vacuum at 120 °C for 24 h. Coin cells were assembled in an argon-filled glove box using a Li foil and polypropylene membrane (Celgard 2400) as counter electrode and separator. The electrolyte was 1.0 M LiPF<sub>6</sub> in a mixture of ethylene carbonate/dimethyl carbonate with a volumetric ratio of 1:1. For the fabrication of LNMO//LTO full cells, the anode to cathode capacity ratio was controlled at 1.1:1 and the rate and specific capacity values of the full cells were calculated based on the cathode mass. Cyclic voltammetry (CV) tests were performed using an Autolab electrochemical workstation with scan rates of 0.1, 0.25, 0.5, 0.75 and 1.0 mV s<sup>-1</sup>. Electrochemical impedance spectrum (EIS) was carried out at frequencies between 10<sup>5</sup> Hz and 10<sup>-2</sup> Hz at open-circuit voltage before the cycling

process. The charge/discharge experiment and long-term stability were carried out with a Maccor Series 4000 Battery Test System in the voltage range 1.0–2.5 V and 3.5–4.9 V for LTO and LNMO based half cells, respectively.

### 3. Results and discussion

In this paper, we prepare the PDG modified Al foil to fabricate the LIBs and the process is schematically shown in Fig. 1. The entire process contains (1) deposition of PAA on the Al foil by the doctor-blade coating method; (2) thermal treatment of the PAA/Al films at 350 °C under a N<sub>2</sub> atmosphere to convert the PAA into PI structure; (3) CO<sub>2</sub> laser irradiation of the PI/Al electrode to transform the PI into PDG; (4 and 5) electrode fabrication and battery assembling process. Here, the PAA was used as PI precursor which was dissolved in NMP (15%) and cast on the Al foil. The deposited PAA film was heated at 100 °C for 60 min to remove the NMP solvent. Then the PAA was imidized into PI film by further hard-curing at 350 °C under a N<sub>2</sub> atmosphere. Finally, the PI/Al electrode was irradiated with CO<sub>2</sub> laser to produce the PDG/Al electrode, which can be directly integrated into the typical fabrication process of LIB.

The GPC profile of the PAA with NMP as an eluent is shown in Fig. 2a to ascertain its molecular weight and molecular weight distribution. According to the analysis of GPC, the weight-average (M<sub>w</sub>) and number-average (M<sub>n</sub>) molecular weights of PAA are 1.90 × 10<sup>5</sup> and 1.68 × 10<sup>5</sup> g mol<sup>-1</sup>, leading to a polydispersity index (PDI) of 1.13. The PDI value is almost close to 1, indicating the good control of the PAA during the polymerization. The inset of Fig. 2a exhibits the deposition of PAA on

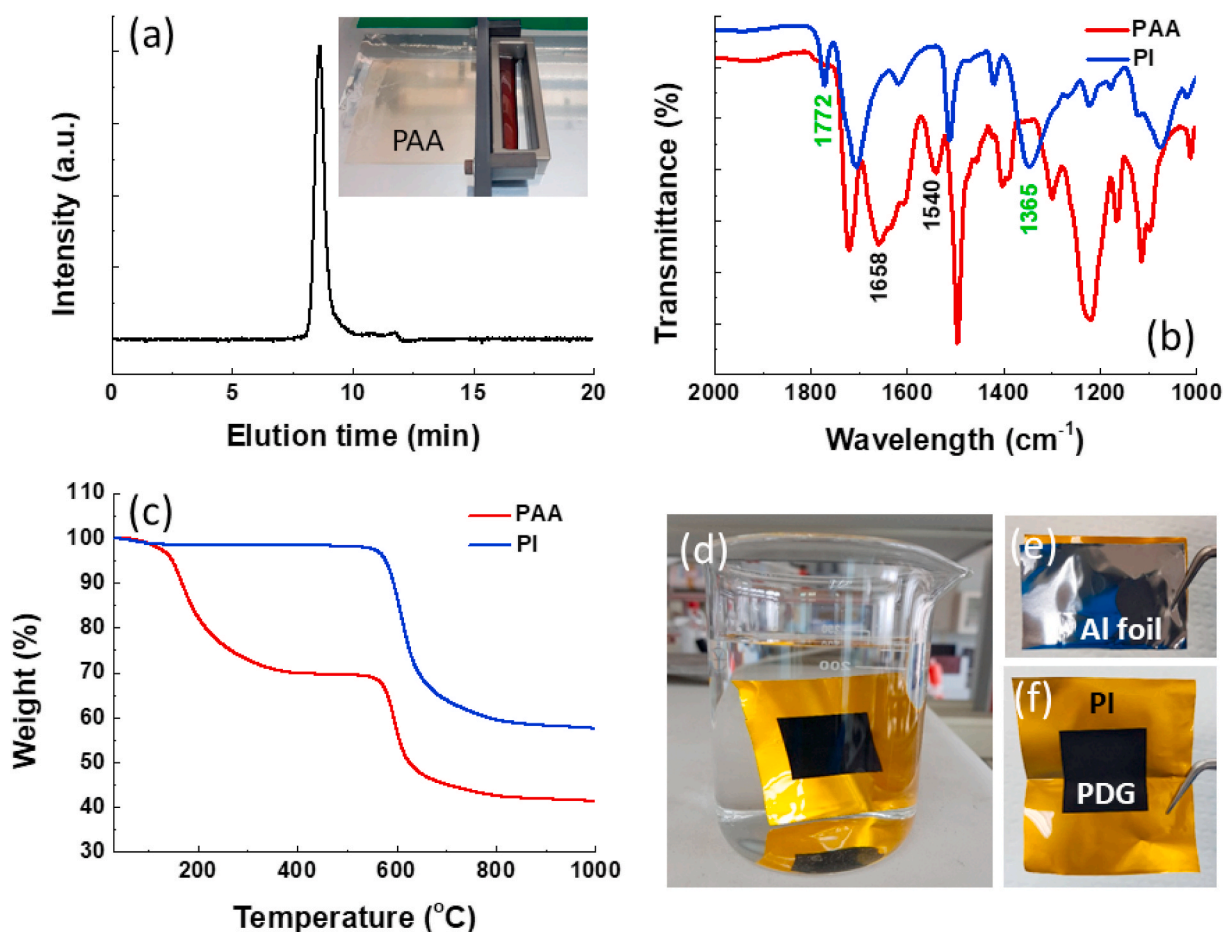


**Fig. 2.** Preparation of the PDG modified Al substrate. (a) GPC profile of the as-prepared PAA; (b) the FTIR spectrum of PAA and PI; (c) the TGA curve of PAA and PI; (d) the evaluation of interfacial adhesion between PDG and Al electrode by immersing the sample in NMP solvent and (e, f) bending and folding the PDG/Al electrode.

the Al foil by the doctor-blade coating process. The thermal imidization reaction of PAA was confirmed by FTIR and TGA analysis. In the FTIR spectrum of PAA (Fig. 2b), characteristic bands at  $1540\text{ cm}^{-1}$  is belonged to C–N stretching mode of amide group, and the signal at  $1658$  and  $1717\text{ cm}^{-1}$  is attributed to the C=O stretching vibration modes of amide and carboxylic acid group in the PAA film [26,27]. After the thermal imidization, the bands at  $1540$  and  $1658\text{ cm}^{-1}$  of PAA disappears and two new bands at  $1365$  and  $1772\text{ cm}^{-1}$  can be observed, which are assigned to C–N vibration from the imide ring and asymmetric stretching modes of CO [28,29]. The Raman spectrum of the as-prepared PI is also provided in the Supporting Information (Fig. S1). The TGA results of PAA and PI measured in nitrogen atmosphere are shown in Fig. 2c. The PAA film reveals two decomposition stages. The first weight loss observed between  $130$  and  $320\text{ }^{\circ}\text{C}$  is contributed from the removal of residual NMP solvent and imidization reaction [30]. The second stage ranged between  $570$  and  $650\text{ }^{\circ}\text{C}$  can be assigned to the thermolysis of PI backbone, which also can be observed in the PI sample. The XRD patterns of the PAA and corresponding PI are also provided in the Supporting Information (Fig. S2). After the thermal treatment, the resultant PI shows an enhanced crystallinity than that of PAA. These results observed in FTIR and TGA analysis suggest that the PAA film was successfully converted to PI after thermal treatment. The interfacial adhesion between the PDG and Al foil was also evaluated by immersing

the sample in NMP solvent. After immersion in NMP for 2 h, the PDG/Al sample still maintains its original state without peeling off the PDG from the substrate as shown in Fig. 2d. Moreover, the PDG/Al substrate still exhibits a complete appearance without damage after bending or folding (Fig. 2e and f).

The top view SEM image of PDG deposited on Al electrode is shown in Fig. 3a. The PDG surface reveals macroporous morphology with sheet- and fiber-like structures. During the laser irradiation, the photothermal process can generate a rapid local heating accompanied with a significant increase in internal pressure due to the release of gaseous production such as  $\text{CO}_2$  and  $\text{H}_2\text{O}$ . The rapid degassing process can result in the expansion of the resultant PDG which transforms the PI into graphene with 3D hierarchical structures. The TEM image of the as-prepared PDG is also shown in Fig. 3b to further investigate its morphology. Sheet-like structure with nanoscale wrinkles can be observed from the PDG indicating the graphene nature of the PDG. The  $\text{N}_2$  adsorption/desorption isotherm of the PDG is presented in Fig. 3c. The porous structure of the PDG with a surface area of  $\sim 290\text{ m}^2/\text{g}$  can create a large interfacial area between the PDG modified layer and active materials leading to better charge transfer. XRD pattern of the PDG is shown in Fig. 3d. In the XRD pattern of PDG, two peaks located at  $25.8^{\circ}$  and  $43.4^{\circ}$  can be noticed, which are typical (002) and (100) reflections of graphene. The strong XRD peak at  $2\theta = 25.8^{\circ}$  corresponds to



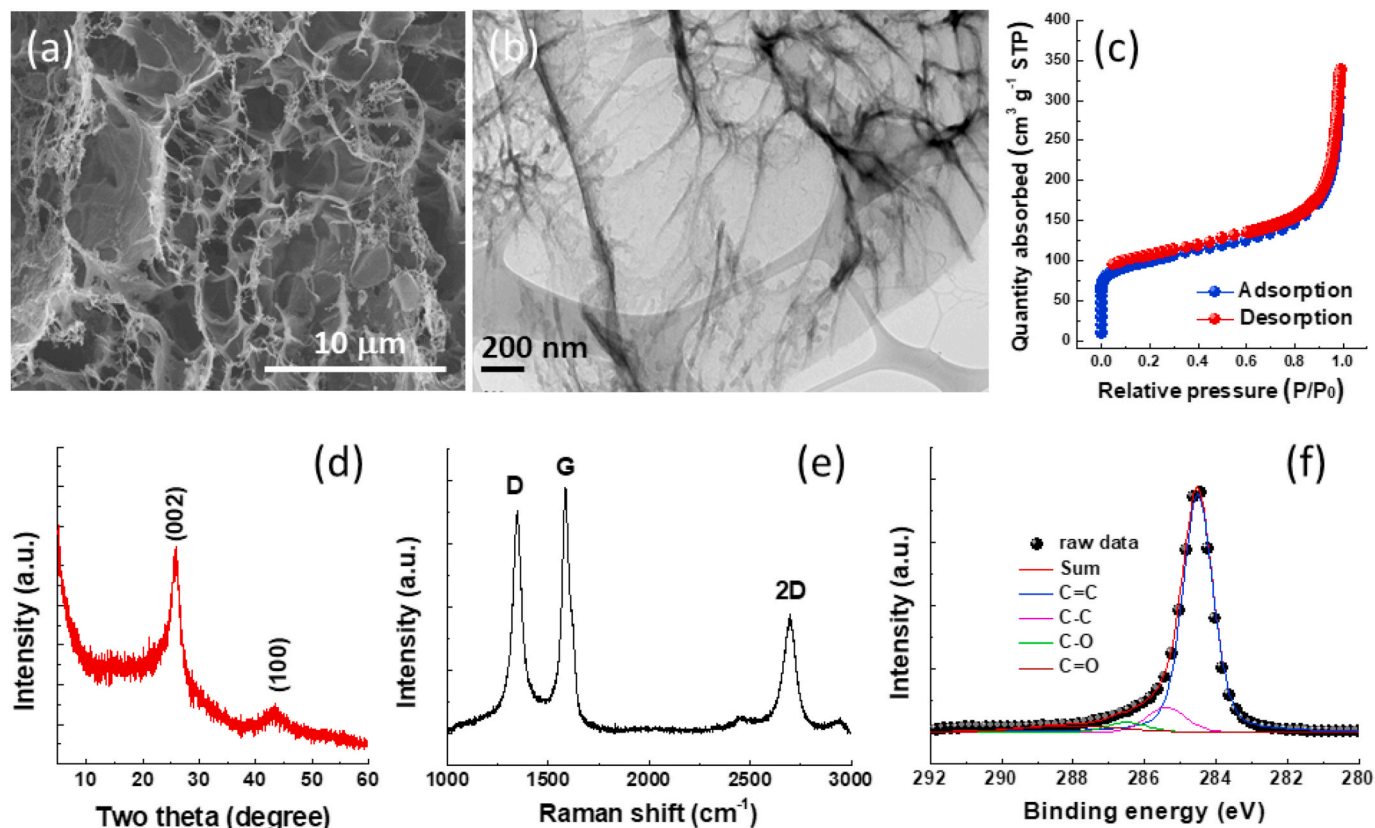


**Fig. 3.** The Characterization of the as-prepared PDG. (a) The SEM image of PDG; (b) the TEM image of PDG; (c) the nitrogen adsorption/desorption isotherms of PDG powder; (d) the XRD pattern of the PDG; (e) Raman spectrum of PDG; (f) the deconvoluted C 1s core level XPS spectrum of PDG.

an interlayer distance of 0.345 nm for the PDG. This result indicates that the PI has been successfully converted into the graphene during the laser irradiation. The Raman spectrum of PDG as shown in Fig. 3e presents three prominent peaks, namely, the D band at around  $1354\text{ cm}^{-1}$  due to the defect and disordered structure [31], the G band at  $1590\text{ cm}^{-1}$  displaying the in-plane bond stretching of  $\text{sp}^2$  carbon in graphene [32] and the 2D peak at  $2698\text{ cm}^{-1}$  emerging from a double resonant scattering phenomenon [33]. The relatively low  $I_D/I_G$  ( $\sim 0.89$ ) indicates that the high structural quality of the as-prepared PDG. The C 1s spectrum of PDG, shown in Fig. 3f can be deconvoluted into the dominant C=C and C-C peaks with greatly suppressed C-O and C=O peaks, suggesting that most of the carbon-oxygen compounds in PI has been removed during the laser irradiation.

To evaluate the effect of PDG on the LIBs, in this study, we assembled the LTO half cells, LNMO half cells and LNMO//LTO full cells using PDG modified Al foil as the current collector. The LTO anode material and LNMO cathode material were prepared from spray-dried and co-precipitation approaches, respectively. The crystal structures of the LTO and LNMO characterized by XRD are displayed in Fig. 4a and b. It is demonstrated that all the peaks in the patterns of anode and cathode materials correspond to the standard LTO (JCPDS No. 26-1198) and LNMO (JCPDS No. 32-0581) cubic spinel structures. The atomic structure of the LTO and LNMO samples was also investigated with Raman spectroscopy. As depicted in Fig. 4c, the LTO reveals typical spinel feature with six Raman phonon modes ( $A_{1g} + E_g + 3F_{2g}$ ) [34]. The signal at  $674\text{ cm}^{-1}$  with a shoulder at  $754\text{ cm}^{-1}$  can be assigned to the vibrations of Ti-O bonds in the  $\text{TiO}_6$  octahedra and the signal located at  $350$

and  $430\text{ cm}^{-1}$  are known as the stretching vibrational mode of Li-O bonds in  $\text{LiO}_4$  tetrahedra. The lower frequency peak at  $231\text{ cm}^{-1}$  corresponds to bending vibrations of O-Ti-O bonds [35]. Fig. 4d displays the Raman spectrum of the LNMO powder. The intense peaks at  $629\text{ cm}^{-1}$  are assigned to the symmetric Mn-O stretching vibration of  $\text{MnO}_6$  octahedra and the peaks at  $484$  and  $397\text{ cm}^{-1}$  can be assigned to the  $\text{Ni}^{2+}$ -O stretching [36]. In addition, the strong peak at  $157\text{ cm}^{-1}$  indicates that the as-prepared LNMO sample is ordered  $\text{P4}_332$  phase. Fig. 4e shows the particle size distributions of the LTO and LNMO ranged between  $1.62$  and  $26.3$  and  $1.42$ – $23.3\text{ }\mu\text{m}$ . Moreover, the mean particle size ( $D_{50}$ ) of the LTO and LNMO powders are  $8.1$  and  $12.1\text{ }\mu\text{m}$ , respectively. The SEM micrographs of the LTO and LNMO are also shown in Fig. 4. Due to the spray-dried process, the LTO powder reveals a microspherical morphology (Fig. 4f) constructed by primary nanoparticles ( $\sim 100\text{ nm}$ ) to form a porous surface (Fig. 4g). The presence of porous structure can increase the interfacial area between the LTO electrode and electrolyte leading to the enhancement in the kinetics of  $\text{Li}^+$  ion intercalation. The SEM morphology of the LNMO obtained from co-precipitation method shows a quasi-spherical structure (Fig. 4h) comprised of densely packed plate-like crystallites. The primary plate-like crystallites with a mean width and length of about  $0.47$  and  $2.27\text{ }\mu\text{m}$ , respectively (Fig. 4i). The dense structure of the LNMO microparticles is originated from the ammonia-induced dissolution-recrystallization process of the initially precipitated mixed Ni-Mn hydroxides due to the tendency to minimize their surface energy [37,38]. The densely packed structure of the LNMO can enhance its tap density, which is favorable for the energy density of the LNMO

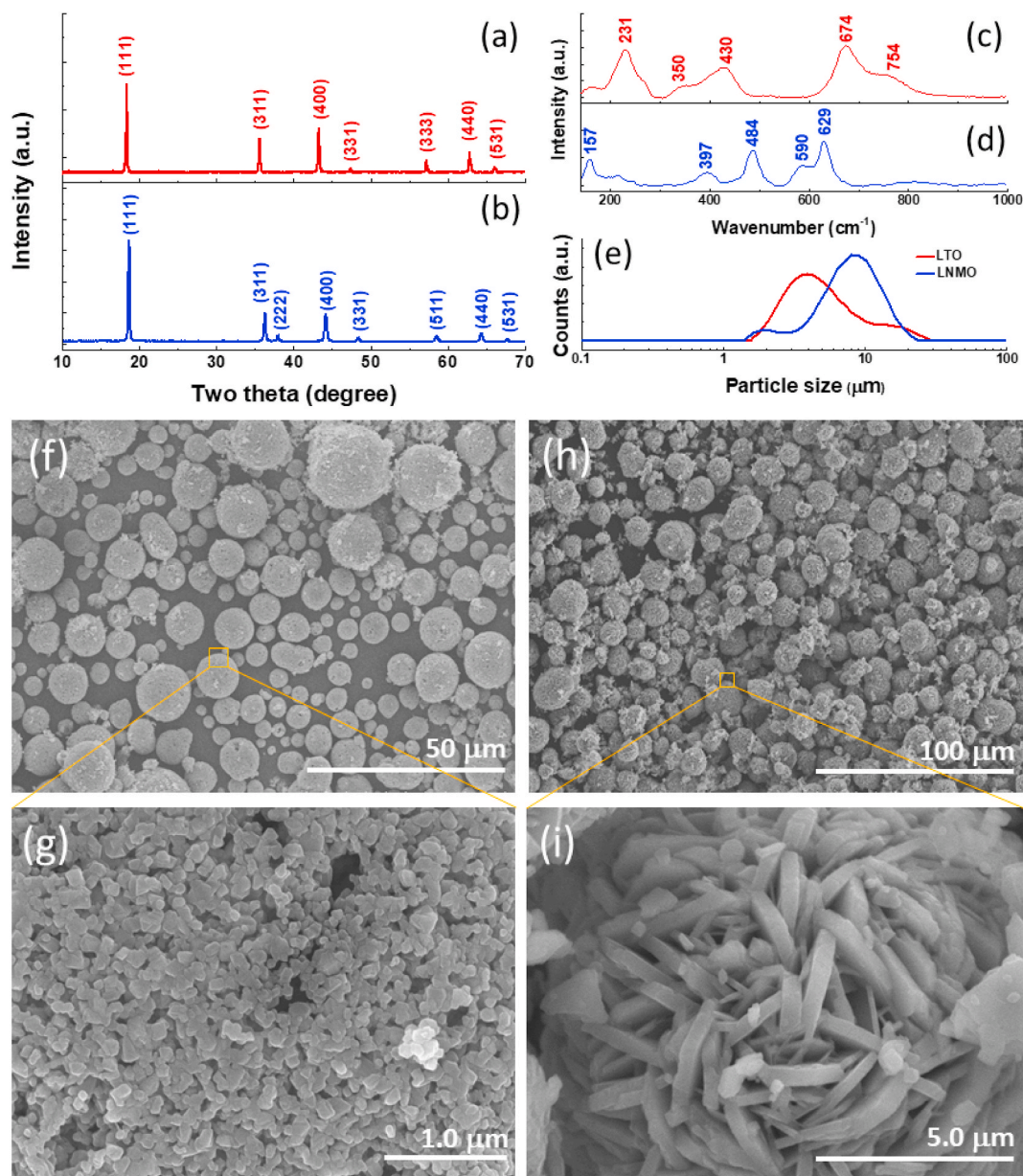


**Fig. 4.** The Characterization of the LTO and LNMO samples. The XRD pattern of (a) LTO and (b) LNMO powders; the Raman spectrum of (c) LTO and (d) LNMO powders; (e) the particle size distribution of the LTO and LNMO powders; (f,g) the SEM image of LTO powder and (h,i) the SEM image of LNMO powder.

cathode-based LIBs.

The cross-sectional SEM images of PI/Al, PDG/Al, LTO-PDG/Al and LTO-Al are shown in Fig. 5. The deposited PI film on Al substrate exhibits a smooth surface with a uniform thickness of around 25  $\mu\text{m}$ . After the laser irradiation, the cross-sectional view of the resultant PDG film indicates that the whole film is constructed by the highly porous graphene sheets (Fig. 5b). Moreover, the PDG film reveals a much larger thickness (37  $\mu\text{m}$ ) than that of PI due to its porous structure. In this study, the obtained PDG/Al substrate was used as current collector to fabricate LIBs. Here, we deposited the LTO on the PDG/Al electrode, followed by calendaring process. The SEM images of the LTO-Al and LTO-PDG/Al are shown in Fig. 5c and d. After the compaction process, the porous PDG film becomes a solid and continuous graphene film with a thickness of  $\sim 3.7 \mu\text{m}$  between LTO and Al electrode. In contrast, the LTO/Al sample only shows a LTO layer on the Al electrode without the PDG buffer layer. The cross-sectional SEM images of LNMO/Al and LNMO-PDG/Al are also shown in the Supporting Information (Fig. S3).

The cycling life and rate performance of LIBs are closely linked to the adhesion strength and interface resistance between the electrode coating and the substrate. Table 1 shows the effect of PDG layer on the adhesion strength, interface resistance and material resistance. The adhesion strength of the LTO to the substrate can be dramatically increased with introducing the PDG layer between the LTO layer and Al electrode. The enhanced attachment is originated from the rough surface of PDG layer with highly porous structure, which can increase the contact area of LTO and the current electrode resulting in better attachment [11,39]. In general, the electrode resistance can be divided into material resistance and interface resistance between the active layer and metal electrode. A. Takeda et al. have successfully individual measured the material resistance of the electrode composite and the interface resistance between the electrode composite and the current collector using the electrode resistance meter (RM2610 HIOKI) [40–42]. Here, we also measure the material resistance and interface resistance of LTO electrode to study the impact of PDG layer on the electronic resistance. The LTO-Al and



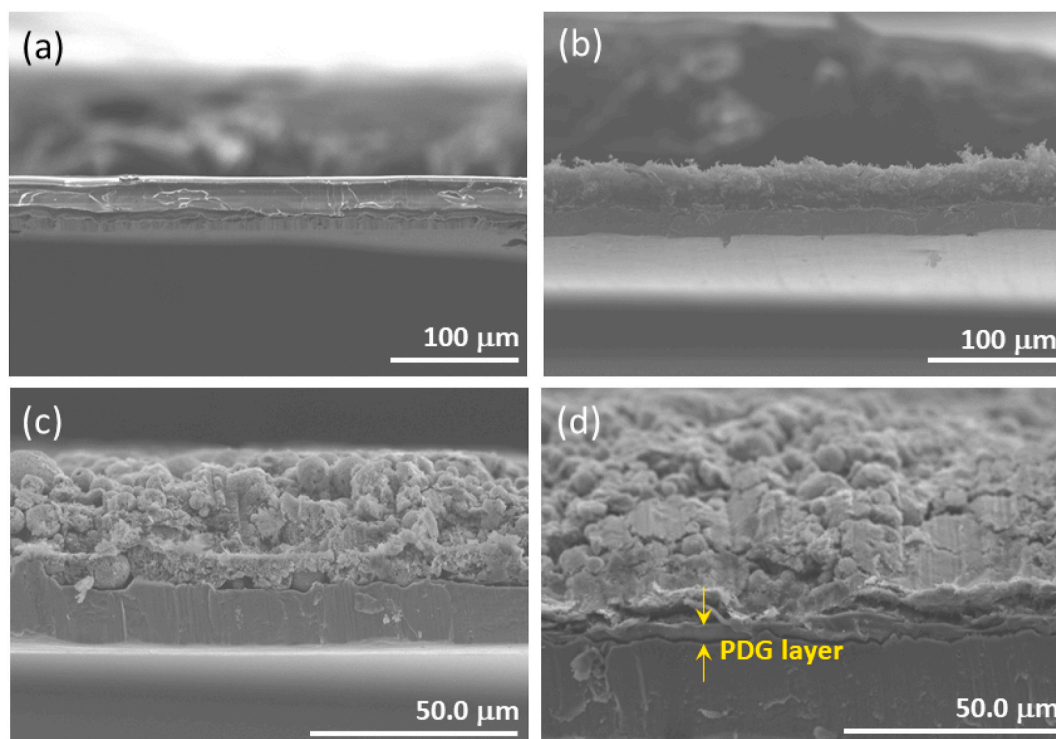


**Fig. 5.** The morphological investigation of the LTO-PDG/Al electrode. The cross-sectional SEM metrology of (a) PI/Al substrate; (b) PDG/Al substrate; (c) LTO-Al electrode; (d) LTO-PDG/Al electrode. It can be seen that the thickness of the inserted PDG layer between LTO layer and Al foil is around 4  $\mu\text{m}$ .

**Table 1**

The adhesion strength, material and interface resistances of LTO-Al and LTO-PDG/Al electrodes.

Electrode	Adhesion strength ( $\text{kgf cm}^{-2}$ )	Material resistance ( $\Omega \text{ cm}^2$ )	Interface resistance ( $\Omega \text{ cm}^2$ )
LTO-Al	0.395	0.184	17.56
LTO-PDG/ Al	0.648	0.188	3.18

LTO-PDG/Al electrodes exhibit a similar material resistance ( $0.184\text{--}0.188 \Omega \text{ cm}^2$ ), indicating the PDG layer cannot alter the electron transfer behavior within the active layer. In contrast, the LTO-PDG/Al shows a much lower interface resistance ( $3.18 \Omega \text{ cm}^2$ ) than that of LTO-Al electrode ( $17.56 \Omega \text{ cm}^2$ ). In addition, the measured material resistance of LTO-PDG/Al is almost 17 times larger than the value of interface resistance. These results imply that the overall electrode resistance is mainly dominated by the interface resistance. Moreover, the inserted PDG layer can offer a better contact between the active material and Al substrate to improve the physical adhesion and reduce the interface resistance. The corresponding parameters of the LNMO-Al and LNMO-PDG/Al are also offered in the Supporting Information (Table S1).

The CV curves of the LTO-Al and LTO-PDG/Al electrode were measured to investigate the effect of PDG modified layer on the electrochemical characteristics of LTO based LIB. Compared with the LTO/Al electrode, the LTO-PDG/Al electrode exhibits a narrow gap between anodic and cathodic peaks with a more intense redox peak (Fig. 6a). The lower polarization of LTO-PDG/Al electrode is mainly attributed to the decrease of electrode resistivity by the insertion of the PDG layer between LTO and Al foil. The EIS results of the LTO-Al and LTO-PDG/Al based cells are shown in Fig. 5b. With fitting the EIS spectrum with the equivalent circuit as shown in the inset, it is found that the charge transfer resistance ( $R_{\text{ct}}$ ) of the LTO-Al and LTO-PDG/Al electrodes is 77.6 and 41.3  $\Omega$ , respectively. The inserted PDG layer can improve the

contact between electrode layer and the current collector leading to lower polarization and  $R_{\text{ct}}$ . Fig. 6c and d compare the charge/discharge profiles of the LTO-Al and LTO-PDG/Al based cells at various rates from 0.1 C to 20 C. Both the samples show a flat voltage plateau at different current densities, which is attributed to a typical character of the  $\text{Li}_4\text{Ti}_5\text{O}_{12}/\text{Li}_7\text{Ti}_5\text{O}_{12}$  two-phase reaction. The plots of polarization ( $\Delta E$ ) vs. rate for the two samples are shown in Fig. 6e. The value of  $\Delta E$  is defined as the difference between the potentials of charge plateaus and discharge plateaus. The LTO-PDG/Al cell exhibits smaller  $\Delta E$  values than the LTO-Al cell at all rates. Moreover, with increasing the rate, the difference between the  $\Delta E$  values in the two cells becomes larger. The rate capabilities of the two samples are shown in Fig. 6f. Obviously, the LTO-PDG/Al electrode reveals a better rate capability than that of LTO-Al sample. The specific capacity of the LTO-PDG/Al electrode recorded at 20 C is  $142 \text{ mAh g}^{-1}$ , while the LTO-Al sample only has  $97.7 \text{ mAh g}^{-1}$ . These results demonstrate that the PDG layer inserted in LIB can significantly reduce its resistance and thus can favor its rate capability. To explore the compatibility between the PDG layer and cathode materials, we also fabricated the LNMO half cells with and without the PDG layer. The comparison of CV curves of the LNMO-Al and LNMO-PDG/Al based half cells is shown in Fig. S4. The LNMO-PDG/Al electrode exhibits a stronger redox peak with a lower degree of polarization, suggesting its lower interface resistance. Furthermore, as shown in Fig. S5, it also shows that the LNMO-PDG/Al electrode can deliver an enhanced rate performance than that of LNMO-Al one. These results suggest that the PDG layer can be effectively integrated into both anode and cathode electrodes.

Full coin cells consisting of the LTO and LNMO as anode and cathode materials were developed to further demonstrate the potential application of the modified Al electrode. The CV curves of LTO-PDG/Al and LNMO-PDG/Al based half cells are exhibited in Fig. 7a. The redox peaks of LTO and LNMO around 1.47–1.63 V and 4.60–4.84 V correspond to the transformation of  $\text{Ti}^{4+}/\text{Ti}^{3+}$  [43] and  $\text{Ni}^{2+}/\text{Ni}^{4+}$  [44], respectively. In general, the working potential can be determined by the intermediate potential between the oxidation and reduction peaks. Therefore, the

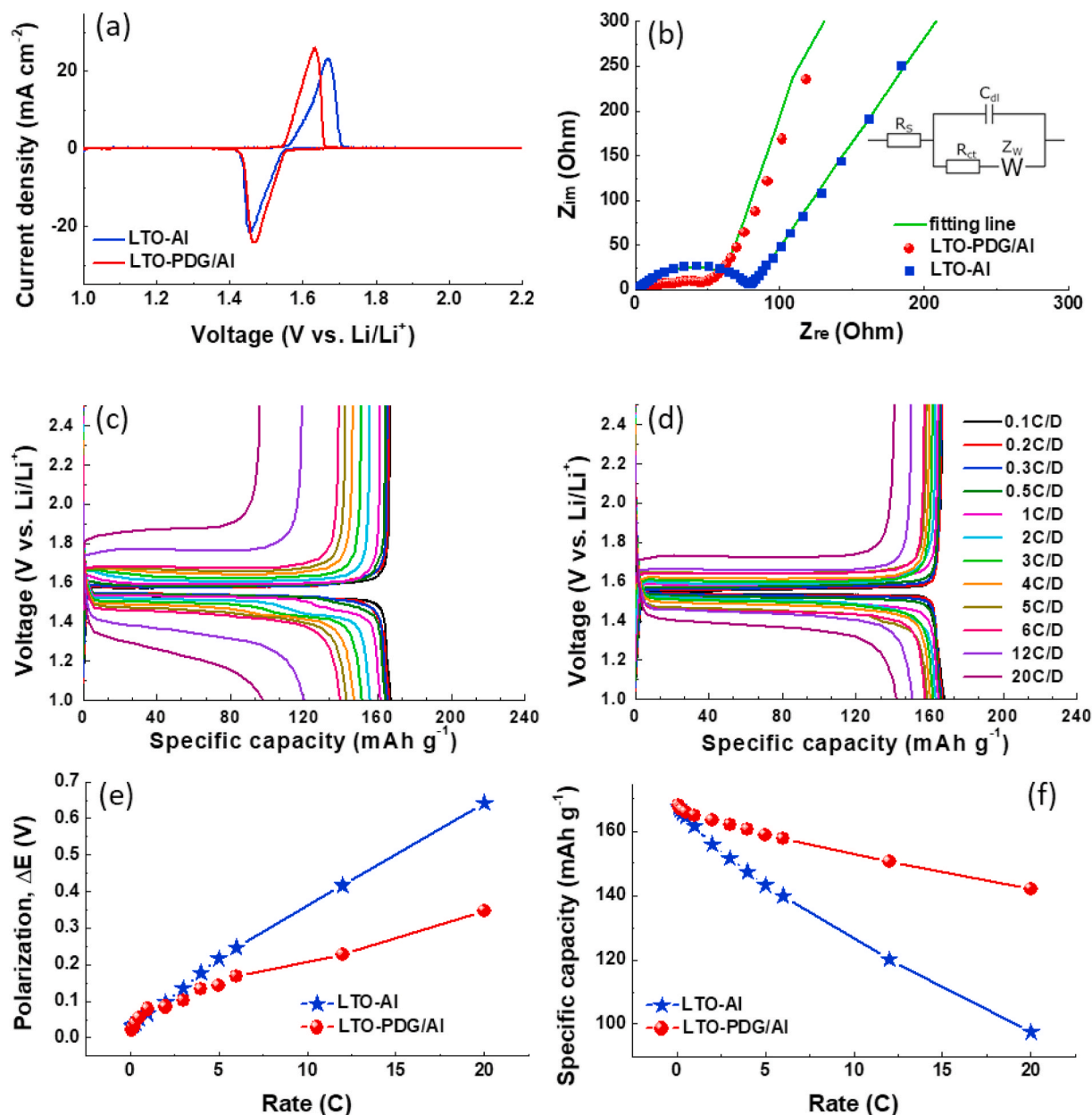


**Fig. 6.** Energy storage performance of the LTO-Al and LTO-PDG/Al based half cells. (a) the CV curve (scan rate:  $0.1 \text{ mV s}^{-1}$ ); (b) the EIS spectrum; galvanostatic charge/discharge curves of (c) LTO-Al electrode; (d) LTO-PDG/Al electrode; (e) plots of  $\Delta E$  versus C rates and (f) rate capability of the LTO-Al and LTO-PDG/Al electrodes.

working potentials of the LTO and LNMO can be calculated to be 1.55 V and 4.72 V, respectively. As a result, the full cells based on the combination of spinel LTO anode and LNMO cathode can deliver a high operating voltage of 3.17 V. The CV curves of the bare (Al-LNMO//LTO-Al) and PDG incorporated cells (Al/PDG-LNMO//LTO-PDG/Al) are shown in Fig. 7b. The redox couple observed in the region of 3.03–3.27 V for both the two cells is contributed from the spinel/rock-salt phase transition of the LTO anode and typical redox transition of the LNMO cathode [45]. Moreover, the PDG modified cell exhibits a sharper profile with a larger current compared with that of bare cell, suggesting its better electrochemical kinetics. The rate capability of the two full cells were measured at a constant charge rate of 0.1C and various discharge rates ranging from 0.1 to 12 C (Fig. 7c). The corresponding charge/discharge profiles of the PDG modified cell are shown in Fig. 7d. The charge/discharge profile of LNMO//LTO full cell exhibits a voltage plateau at approximately 3.1 V during discharge, which corresponds to

the  $\text{Ni}^{2+}/\text{Ni}^{4+}$  redox [46]. As shown in Fig. 7c, the full cell with PDG layer can deliver an enhanced rate capability than that of pristine one, which agrees with the behavior of half cells. The specific capacities of the PDG incorporated cell are calculated to be 115.0, 109.9, 102.6, 96.4, 88.5 and 78.1  $\text{mAh g}^{-1}$  at discharge rates of 0.1, 1, 3, 5, 8 and 12 C, respectively. The charge/discharge curves of the bare LNMO//LTO full cell are also provided in the Supporting Information (Fig. S6).

To prolong the life and optimize the energy usage of LIBs, it is necessary to maintain the operating temperature of the LIB within a narrow range. In the present work, the soft-packed LTO//LNMO full cells with and without PDG layer were also assembled to monitor the temperature rise of the cells during charging and discharging, as shown in the inset of Fig. 8a (The inset of Fig. 8a shows the photograph of the soft-packed cell and the LIB electrodes are located at the red marked region.). The temperature rises and distribution of the modified cell and pristine cells were observed by an infrared camera. The temperature of



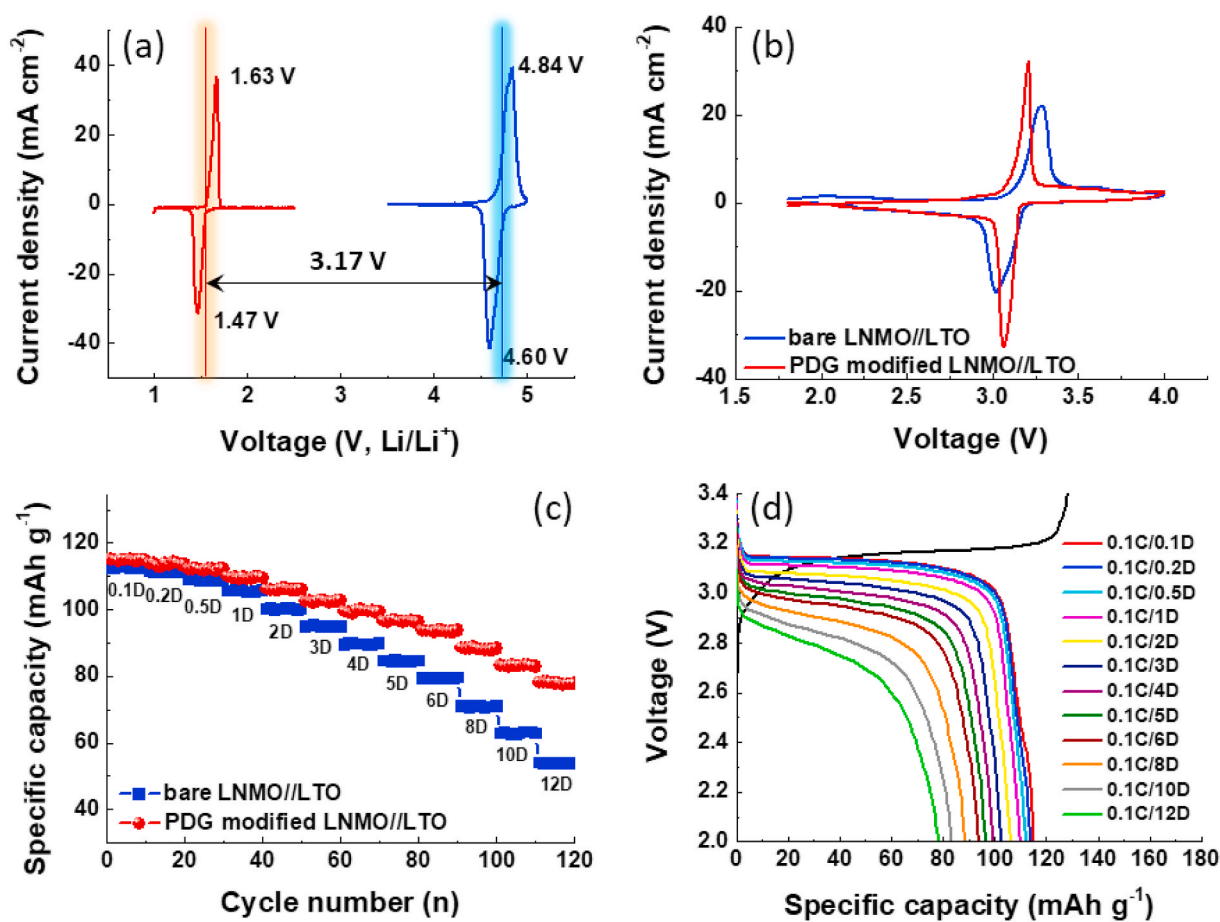


**Fig. 7.** Fabrication of the Al/PDG-LNMO//LTO-PDG/Al full cell. (a) typical CV curve of the LTO and LNMO based half cells; (b) the CV profiles of the LNMO//LTO full cells with and without the PDG layer; (c) the rate capability of the bare and PDG incorporated LNMO//LTO full cells; (d) the corresponding charge/discharge profiles of the PDG incorporated LNMO//LTO full cell at a constant charge rate of 0.1 C and various discharge rates.

the full cells was recorded after 20 repeated charge/discharge cycles. As shown in Fig. 8a, with increasing the C rates, both the two kinds of cells exhibit an increase in temperature rise. However, the PDG inserted cell still can reveal a lower temperature rise under various rates. The corresponding IR-image of two cells captured at different C-rates is also shown in Fig. 8b. These IR-images demonstrate the both the two cells show a uniform temperature distribution without any hotspots. Fig. 8c reveals the cycling performance of the full coin cells with and without PDG layer measured at 5C for 500 cycles. A capacity retention of 95.9% is observed for the PDG modified cell, which is better than that of the pristine cell (88.8%). The enhanced temperature rises and cycling performance of the PDG modified cell is originated from its lower interface resistance and polarization. Moreover, we also compared the cycling performance of the PDG modified cell at 1, 5 and 10 C as shown in Fig. 8d. The PDG modified cell delivers a specific capacity of 109.9, 96.1 and 82.6  $\text{mAh g}^{-1}$  at 1, 5 and 10 C in the first cycle, and a value of 108.3, 92.2 and 70.0  $\text{mAh g}^{-1}$  after 500 cycles, leading a capacity retention of 98.5, 95.9, and 84.7%, respectively. Such excellent electrochemical performance can be attributed to the successful integration of the PDG layer with the anode and cathode electrodes resulting in an improved rate capability and long-term stability.

#### 4. Conclusion

In this article, we have successfully prepared the PDG modified Al electrode which can be used as current collector for improving the performance of LIBs. The inserted PDG layer can provide a larger contact

area between the active layer and electrode due to its 3D porous architecture. The better contact can enhance the physical adhesion and reduce the interface resistance between the active layer and electrode. Electrochemical characterizations revealed that the LNMO//LTO full cells fabricated with the PDG layer show superior rate performance with a discharge capacity of 115.7  $\text{mAh g}^{-1}$  at 1 C. Meanwhile, the PDG incorporated cells also reveal remarkable capacity retention of 98.5% after 500 cycles. The prominent performances is ascribed to the improvement in the lower polarization temperature rise by introduction of the PDG layer. These results demonstrate that PDG/Al electrode can be utilized as a potential current collector of high-performance LIBs.

#### CRediT authorship contribution statement

**Er-Chieh Cho:** Writing – original draft, Methodology. **Cai-Wan Chang-Jian:** Synthesis, laser process. **Yen-Ju Wu:** Calculation, SEM. **Szu-Han Chao:** Raman analysis, Formal analysis. **Jen-Hsien Huang:** Software, Validation. **Kuen-Chan Lee:** Synthesis, Conceptualization. **Huei Chu Weng:** Battery assembly and testing. **Shih-Chieh Hsu:** Supervision, Conceptualization, Writing – review & editing.

#### Declaration of competing interest

The authors declare that they have no known competing financial interests or personal relationships that could have appeared to influence the work reported in this paper.

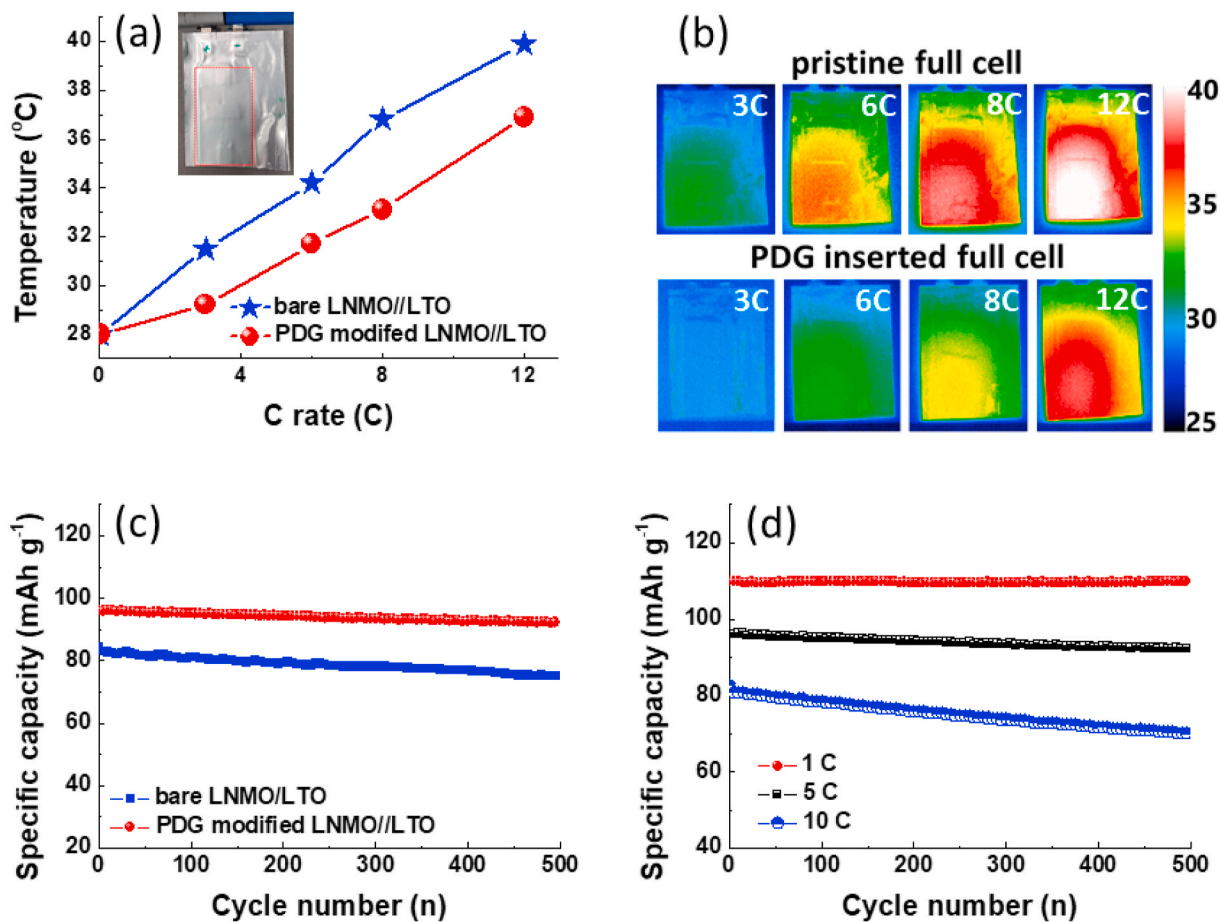


**Fig. 8.** The effect of PDG layer on the cycling life of the LNMO//LTO full cell. (a) the temperature rise of the LNMO//LTO full cells stepped at different C rates (The inset shows the photograph of the soft-packed cell); (b) the thermal-imaging photograph of the full cells with and without PDG layer captured from various C rates; (c) the cycle performance of the full coin cells with and without PDG layer tested at 5 C; (d) the cycle performance of the PDG incorporated full coin cell tested at 1, 5 and 10 C for 500 cycles.

## Acknowledgment

We are grateful to the Ministry of Science and Technology (MOST 108-2320-B-038-043), (MOST 108-2113-M152-001) and (MOST 108-2221-E-032-031-) for financial support.

## Appendix A. Supplementary data

Supplementary data to this article can be found online at <https://doi.org/10.1016/j.jpowsour.2021.230060>.

## References

- [1] S.O. Amrouche, D. Rekioua, T. Rekioua, S. Bacha, Overview of energy storage in renewable energy systems, *Int. J. Hydrogen Energy* 41 (2010) 20914–20927.
- [2] A. Barré, B. Deguilhem, S. Grolleau, M. Gérard, F. Suard, D. Riu, A review on lithium-ion battery ageing mechanisms and estimations for automotive applications, *J. Power Sources* 241 (2013) 680–689.
- [3] M.A. Hannan, M.S.H. Lipu, A. Hussain, A. Mohamed, A review of lithium-ion battery state of charge estimation and management system in electric vehicle applications: challenges and recommendations, *Renew. Sustain. Energy Rev.* 78 (2017) 834–854.
- [4] H.C. Hesse, M. Schimpe, D. Kucevic, A. Jossen, Lithium-Ion Battery Storage for the Grid—a review of stationary battery storage system design tailored for applications in modern power grids, *Energies* 10 (2017) 2107.
- [5] F. Li, Y. Gong, G. Jia, Q. Wang, Z. Peng, W. Fan, B. Bai, A novel dual-salts of LiTFSI and LiODFB in LiFePO<sub>4</sub>-based batteries for suppressing aluminum corrosion and improving cycling stability, *J. Power Sources* 295 (2015) 47–54.
- [6] M. Kazazi, M.R. Vaezi, A. Kazemzadeh, Improving the self-discharge behavior of sulfur-polypyrrole cathode material by LiNO<sub>3</sub> electrolyte additive, *Ionics* 20 (2014) 1291–1300.
- [7] A. Moretti, G.T. Kim, D. Bresser, K. Renger, E. Paillard, R. Marassi, M. Winter, S. Passerini, Investigation of different binding agents for nanocrystalline anatase TiO<sub>2</sub> anodes and its application in a novel, green lithium-ion battery, *J. Power Sources* 221 (2013) 419–426.
- [8] X. Tong, F. Zhang, B. Ji, M. Sheng, Y. Tang, Carbon-coated porous aluminum foil anode for high-rate, long-term cycling stability, and high energy density dual-ion batteries, *Adv. Mater.* 28 (2016) 9979–9985.
- [9] M. Kuenzel, D. Bresser, G.T. Kim, P. Axmann, M. Wohlfahrt-Mehrens, S. Passerini, Unveiling and amplifying the benefits of carbon-coated aluminum current collectors for sustainable LiNi<sub>0.5</sub>Mn<sub>1.5</sub>O<sub>4</sub> cathodes, *ACS Appl. Energy Mater.* 3 (2020) 218–230.
- [10] D. Lepage, L. Savignac, M. Saulnier, S. Gervais, S.B. Schougaard, Modification of aluminum current collectors with a conductive polymer for application in lithium batteries, *Electrochem. Commun.* 102 (2019) 1–4.
- [11] T. Li, H. Bo, H. Cao, Y. Lai, Y. Liu, Carbon-coated aluminum foil as current collector for improving the performance of lithium sulfur batteries, *Int. J. Electrochem. Sci.* 12 (2017) 3099–3108.
- [12] H.C. Wu, H.C. Wu, E. Lee, N.L. Wu, High-temperature carbon-coated aluminum current collector for enhanced power performance of LiFePO<sub>4</sub> electrode of Li-ion batteries, *Electrochem. Commun.* 12 (2010) 488–491.
- [13] K. Striebel, J. Shim, A. Sierra, H. Yang, X.Y. Song, R. Kostecki, K. McCarthy, The development of low cost LiFePO<sub>4</sub>-based high power lithium-ion batteries, *J. Power Sources* 146 (2005) 33–38.
- [14] K. Rytel, D. Waszak, K. Kędzierski, D. Wróbel, Novel method of current collector coating by multiwalled carbon nanotube Langmuir layer for enhanced power performance of LiMn<sub>2</sub>O<sub>4</sub> electrode of Li-ion batteries, *Electrochim. Acta* 222 (2016) 921–925.
- [15] X. Li, S. Deng, M.N. Banis, K. Doyle-Davis, D. Zhang, T. Zhang, J. Yang, R. Divigalpitiya, F. Brandys, R. Li, X. Sun, Suppressing corrosion of aluminum foils via highly conductive graphene-like carbon coating in high-performance lithium-based batteries, *ACS Appl. Mater. Interfaces* 11 (2019) 32826–32832.
- [16] J.M. Jiang, P. Nie, B. Ding, W.X. Wu, Z. Chang, Y.T. Wu, H. Dou, X.G. Zhang, Effect of graphene modified Cu current collector on the performance of Li<sub>4</sub>Ti<sub>5</sub>O<sub>12</sub> anode for lithium-ion batteries, *ACS Appl. Mater. Interfaces* 8 (2016) 30926–30932.

- [17] K. Wang, C. Wang, H. Yang, X. Wang, F. Cao, Q. Wu, H. Peng, Vertical graphene nanosheets modified Al current collectors for high-performance sodium-ion batteries, *Nano Res.* 13 (2020) 1948–1954.
- [18] S.Y. Kim, Y.I. Song, J.H. Wee, C.H. Kim, B.W. Ahn, J.W. Lee, S.J. Shu, M. Terrones, Y.A. Kim, C.M. Yang, Few-layer graphene coated current collectors for safe and powerful lithium ion batteries, *Carbon* 153 (2019) 495–503.
- [19] J. Lin, Z. Peng, Y. Liu, F. Ruiz-Zepeda, R. Ye, E.L.G. Samuel, M.J. Yacamán, B. I. Yakobson, J.M. Tour, Laser-induced porous graphene films from commercial polymers, *Nat. Commun.* 5 (2014) 5714.
- [20] R. Ye, D.K. James, J.M. Tour, Laser-induced graphene, *Acc. Chem. Res.* 51 (2018) 1609–1620.
- [21] J. Rodrigues, J. Zanoni, G. Gaspar, A.J.S. Fernandes, A.F. Carvalho, N.F. Santos, T. Monteiro, F.M. Costa, ZnO decorated laser-induced graphene produced by direct laser scribing, *Nanoscale Adv.* 1 (2019) 3252–3268.
- [22] M.R. Bobinger, F.J. Romero, A. Salinas-Castillo, M. Becherer, P. Lugli, D. P. Morales, N. Rodríguez, A. Rivadeneyra, Flexible and robust laser-induced graphene heaters photothermally scribed on bare polyimide substrates, *Carbon* 144 (2019) 116–126.
- [23] J. Dong, G. Ji, G. Xue, Studies of polyimide/hopper interface and its improvement by a two-component primer, *Macromol. Mater. Eng.* 230 (1995) 143–157.
- [24] K.C. Hsiao, S.C. Liao, J.M. Chen, Microstructure effect on the electrochemical property of  $\text{Li}_4\text{Ti}_5\text{O}_{12}$  as an anode material for lithium-ion batteries, *Electrochim. Acta* 53 (2008) 7242–7247.
- [25] W.K. Pang, H.F. Lin, V.K. Peterson, C.Z. Lu, C.E. Liu, S.C. Liao, J.M. Chen, Enhanced rate-capability and cycling-stability of 5 V  $\text{SiO}_2$ - and polyimide-coated cation ordered  $\text{LiNi}_{0.5}\text{Mn}_{1.5}\text{O}_4$  lithium-ion battery positive electrodes, *J. Phys. Chem. C* 121 (2017) 3680–3689.
- [26] L. Wang, L. Cui, Y. Liu, Electrospun polyimide nanofiber-coated polyimide nonwoven fabric for hot gas filtration, *Adsorpt. Sci. Technol.* 36 (2018) 1734–1743.
- [27] Y.J. Kim, S.J. Yu, Y.G. Jeong, Carbon nanotube/polyimide bilayer thin films with high structural stability, optical transparency, and electric heating performance, *RSC Adv.* 6 (2016) 30106–30114.
- [28] S. Kim, K.S. Jang, H.D. Choi, S.H. Choi, S.J. Kwon, I.D. Kim, J.A. Lim, J.M. Hong, Porous polyimide membranes prepared by wet phase inversion for use in low dielectric applications, *Int. J. Mol. Sci.* 14 (2013) 8698–8707.
- [29] J. Hou, W. Jang, S. Kim, J.H. Kim, H. Byun, Rapid formation of polyimide nanofiber membranes via hot-press treatment and their performance as Li-ion battery separators, *RSC Adv.* 8 (2018) 14958–14966.
- [30] C. Simón-Herrero, X.Y. Chen, M.L. Ortiz, A. Romero, J.L. Valverde, L. Sánchez-Silva, Linear and crosslinked polyimide aerogels: synthesis and characterization, *J. Mater. Res. Technol.* 8 (2019) 2638–2648.
- [31] M.A. Pimenta, G. Dresselhaus, M.S. Dresselhaus, L.G. Cancado, A. Jorio, R. Saito, Studying disorder in graphite-based systems by Raman spectroscopy, *Phys. Chem. Chem. Phys.* 9 (2007) 1276–1290.
- [32] O. Jankovský, P. Šimek, J. Luxa, D. Sedmidubský, I. Tomandl, A. Macková, R. Mikšová, P. Malinský, M. Pumera, Z. Sofer, Inside cover: definitive insight into the graphite oxide reduction mechanism by deuterium labeling, *ChemPlusChem* 80 (2015) 1366.
- [33] X. Wang, J.W. Christopher, A.K. Swan, 2D Raman band splitting in graphene: charge screening and lifting of the K-point Kohn anomaly, *Sci. Rep.* 7 (2017) 13539.
- [34] K. Mukai, Y. Kato, H. Nakano, Understanding the zero-strain lithium insertion scheme of  $\text{Li}[\text{Li}_{1/3}\text{Ti}_{5/3}]\text{O}_4$ : structural changes at atomic scale clarified by Raman spectroscopy, *J. Phys. Chem. C* 118 (2014) 2992–2999.
- [35] C.K. Lan, S.I. Chuang, Q. Bao, Y.T. Liao, J.G. Duh, One-step argon/nitrogen binary plasma jet irradiation of  $\text{Li}_4\text{Ti}_5\text{O}_{12}$  for stable high-rate lithium ion battery anodes, *J. Power Sources* 275 (2015) 660–667.
- [36] J. Zheng, J. Xiao, X. Yu, L. Kovarik, M. Gu, F. Omenya, X. Chen, X.Q. Yang, J. Liu, G.L. Graff, M.S. Whittingham, J.G. Zhang, Enhanced  $\text{Li}^+$  ion transport in  $\text{LiNi}_{0.5}\text{Mn}_{1.5}\text{O}_4$  through control of site disorder, *Phys. Chem. Chem. Phys.* 14 (2012) 13515–13521.
- [37] A. van Bommel, J.R. Dahn, Synthesis of Spherical and Dense Particles of the Pure Hydroxide Phase  $\text{Ni}_{1/3}\text{Mn}_{1/3}\text{Co}_{1/3}(\text{OH})_2$ , vol. 156, 2009, pp. A362–A365.
- [38] F. Zhou, X. Zhao, A. van Bommel, A.W. Rowe, J.R. Dahn, Coprecipitation synthesis of  $\text{Ni}_x\text{Mn}_{1-x}(\text{OH})_2$  mixed hydroxides, *Chem. Mater.* 22 (2010) 1015–1021.
- [39] W. Haselrieder, B. Westphal, H. Bockholt, A. Diener, S. Höft, A. Kwade, Measuring the coating adhesion strength of electrodes for lithium-ion batteries, *Int. J. Adhesion Adhes.* 60 (2015) 1–8.
- [40] A. Takeda, T. Nakamura, H. Yokouchi, H. Tomozawa, Resistance reduction effect by SDX® in lithium-ion batteries, *ECS Trans.* 80 (2017) 283–290.
- [41] Y. Arai, M. Kunisawa, T. Yamaguchi, H. Yokouchi, A. Matsuo, M. Ohmori, Studies of SDXTM on the boundary resistance between aluminum current collectors and cathode active material layers, *ECS Trans.* 50 (2013) 153–160.
- [42] A. Takeda, T. Nakamura, H. Yokouchi, H. Tomozawa, The mechanism of decreasing resistance by SDXTM in lithium ion battery, *ECS Trans.* 75 (2017) 17–25.
- [43] S. Chen, Y. Xin, Y. Zhou, Y. Ma, H. Zhou, L. Qi, Self-supported  $\text{Li}_4\text{Ti}_5\text{O}_{12}$  nanosheet arrays for lithium ion batteries with excellent rate capability and ultralong cycle life, *Energy Environ. Sci.* 7 (2014) 1924–1930.
- [44] B. Xiao, J. Liu, Q. Sun, B. Wang, M.N. Banis, D. Zhao, Z. Wang, R. Li, X. Cui, T. K. Sham, X. Sun, Unravelling the role of electrochemically active  $\text{FePO}_4$  coating by atomic layer deposition for increased high-voltage stability of  $\text{LiNi}_{0.5}\text{Mn}_{1.5}\text{O}_4$  Cathode material, *Adv. Sci.* 2 (2015), 1500022.
- [45] H.F. Xiang, X. Zhang, Q.Y. Jin, C.P. Zhang, C.H. Chen, X.W. Ge, Effect of capacity matchup in the  $\text{LiNi}_{0.5}\text{Mn}_{1.5}\text{O}_4/\text{Li}_4\text{Ti}_5\text{O}_{12}$  cells, *J. Power Sources* 183 (2008) 355–360.
- [46] J. Zheng, J. Xiao, Z. Nie, J.G. Zhang, Lattice  $\text{Mn}^{3+}$  behaviors in  $\text{Li}_4\text{Ti}_5\text{O}_{12}/\text{LiNi}_{0.5}\text{Mn}_{1.5}\text{O}_4$  full cells, *J. Electrochem. Soc.* 160 (2013) A1264–A1268.